Journal of Materials Chemistry A

ROYAL SOCIETY OF CHEMISTRY

PAPER

View Article Online
View Journal

Cite this: DOI: 10.1039/d2ta03932j

Ideal dopant to increase charge separation efficiency in hematite photoanodes: germanium†

Murillo Henrique de Matos Rodrigues, [ab] Ingrid Rodriguez-Gutierréz, [bc] Carlos Alberto Ospina Ramirez,[b] Carlos Alberto Rodrigo Costa,[b] Cleyton Alexandre Biffe,[b] João Batista de Souza Junior, [b] Flavio Leandro Souza [bc] and Edson Roberto Leite *[ab]

Hematite, owing to its ideal physical properties, chemical stability, and abundance on Earth, has become a potential candidate as a photoanode in solar water-splitting device applications. However, the high photogenerated charge recombination due to its low efficiency of charge separation as a consequence of poor electronic transport and collection at the back contact has hindered its commercial application. Based on the limitations of hematite, this study describes germanium as a potentially ideal element that combines the beneficial improvement in charge transfer efficiency and morphology control toward high hematite-based photoanode performance. Intensity-modulated photocurrent spectroscopy results demonstrated that the addition of Ge enhanced the charge mobility, leading to a superior charge separation efficiency compared to the pristine hematite photoanode. C-AFM measurements demonstrate that Ge improves the electronic conductivity and increases the majority carrier mobility. Photoelectrochemical measurements performed at different wavelengths show the Ge interferes with the formation of small polarons, making the charges more mobile (delocalized), thus favoring the process of photoinduced charge separation. The combined role played by Ge addition resulted in a significant improvement in the photoelectrochemical performance from 0.5 to 3.2 mA cm^{-2} at 1.23 V_{RHE} by comparing the pristine and Ge–hematite-based photoanodes.

Received 16th May 2022
Accepted 8th June 2022

DOI: 10.1039/d2ta03932j

rsc.li/materials-a

Introduction

The storage of solar energy as a hydrogen fuel, obtained from water splitting through a photoelectrochemical cell (PEC), can provide a clean and renewable energy alternative for the increasing demand of the world.[1,2] However, to reach competitive levels, PEC-based devices depend on robust and efficient semiconductors (n-type semiconductors, for instance) formed by abundant elements on our planet and with adequate bandgap positions to absorb solar radiation. Hematite (α-Fe_2O_3) satisfies most of these requirements for use as a photoanode in PEC device applications. However, owing to recombination processes between photogenerated pairs of electrons (e^-) and holes (h^+) that occur at the surface, bulk, and semiconductor–electrolyte interface, the efficiency of the hematite photoanode is still far less than the theoretically predicted value.[3] In the last decades, intense studies have been devoted to surpassing the aforementioned limitations by employing a complex rational design mainly involving multiple modifications[4,5] that caused the photocurrent response to exceed values of 3.0 mA cm^{-2} at 1.23 V_{RHE}.[6–11] These modifications include doping, deposition of an overlayer to act as a passivating or co-catalyst layer, formation of heterojunctions on the electrode surface, morphology control, and optimization of the hematite/substrate interface (transparent conductive oxide).[4,5,12]

Several attempts dedicated to improving the performance of hematite photoanodes have focused on charge transfer processes in the liquid–semiconductor interface of PEC devices, that is, they have been concerned with minority charge carriers (h^+).[5,12,13] Doping is a mechanism that aims to improve electronic transport and acts on the majority of charge carriers (e^-) in an n-type semiconductor. The increase in electronic conductivity is a rational way to design highly active hematite photoanodes because it increases the extraction of electrons in back-contact electrodes (transparent conductor oxide materials), resulting in an increase of the charge separation efficiency (CSE) between e^- and h^+.

The doping of foreign atoms, such as groups IV and XIV of the periodic table, into the hematite lattice has been extensively discussed in previous studies.[3–5,14,15] However, there is no consensus on how dopants work to improve the performance of

[a]Departamento de Química, Universidade Federal de São Carlos, 13565-905, Brazil
[b]Laboratório Nacional de Nanotecnologia (LNNano), CNPEM, 13083-100, Brazil. E-mail: edson.leite@lnnano.cnpem.br
[c]Centro de Ciências Naturais e Humanas, Universidade Federal do ABC, 09606-070, Brazil

† Electronic supplementary information (ESI) available. See https://doi.org/10.1039/d2ta03932j

photoanodes. It is common to find experimental results demonstrating that hematite doping does not increase the donor density (N_d) in the literature.[3,16,17]

Perhaps the origin of the lack of agreement on the action mechanism of dopants lies in the fact that small polaron hopping determines carrier transport and limits electron transport in α-Fe_2O_3.[18] Furthermore, as discovered by Leone *et al.*,[19] the small-polaron localization of photoexcited carriers is wavelength-dependent. Small polarons can be efficiently formed near the band-edge excitation, resulting in fewer mobile carriers. However, fewer polarons are generated through higher-energy excitation, resulting in more mobile carriers and a longer lifetime.[19] A clear relationship is observed between the charge carrier mobility and optical properties, which leads us to believe that the function of some dopants is to increase the mobility of charge carriers and not their concentration. Another reason for the lack of agreement on the action of dopants is the strong dependence of foreign atom incorporation in the hematite lattice on the photoanode synthesis method. As discussed recently by Souza Junior *et al.*, the protocol used to incorporate dopants has a strong impact on the performance of PEC devices.[20] In addition to its beneficial effects, the doping of hematite also has side effects, such as surface states, which modify the electrochemical properties of the pristine hematite (mainly the flat band potential (V_{fb}) and charge transfer resistance). The formation of surface states occurs because of the segregation of dopants on the hematite surface.[21,22]

Several prior publications have reported the incorporation of additives in hematite films and demonstrated that the segregation of these elements is a critical factor for improving the photoelectrochemical properties.[21–24] For instance, the segregation of Sb and Sn at solid–solid interfaces (grain boundaries) decreases the grain boundary resistance, facilitating electronic transport and consequently increasing the conductivity of hematite.[23,24] Recently, several theoretical and experimental studies have highlighted the beneficial effect of germanium (Ge) as an additive to improve the photocurrent of hematite photoanodes.[25–31] After analyzing the experimental studies, we observed a clear dependence of the photoelectrochemical performance of the hematite photoanodes on the synthesis route used to introduce Ge.[31] This dependence is associated with the low chemical compatibility between α-Fe_2O_3 and GeO_2.[32] As shown in the phase diagram of this binary system (Fig. S1 in the ESI†), at equilibrium, Ge is not soluble in the hematite lattice and *vice versa*. Thus, from thermodynamic arguments, we expect the segregation and formation of Ge clusters.[30–32] The low reactivity between α-Fe_2O_3 and GeO_2 made us to believe that to maximize the benefits of Ge, it is necessary to use synthetic routes that enable the control of Ge incorporation, generating a metastable solid solution.

In this study, we explore two different approaches that lead to greater control of Ge incorporation in the hematite photoanode. These approaches are combined with a colloidal nanocrystal deposition (CND) process using magnetite nanocrystals (Fe_3O_4) as the α-Fe_2O_3 precursor.[21,22,33] Photoanodes prepared through this novel strategy were systematically characterized to evaluate the role of the additive and its impact on sunlight-driven water oxidation. We will demonstrate that Ge, owing to its chemical characteristics, will act as an "ideal dopant" to increase the CSE of hematite photoanodes. We coined the term "ideal dopant" to describe a dopant that increases the efficiency of the charge separation process by acting on the majority of the charge carriers with minimum interference in the charge transfer process at the semiconductor–electrolyte interface. In previous works, we described that dopant such as Sn and Sb also promote a better charge separation process, improving the hematite photoanode performance.[21,22] However, these dopants promote the formation of surface states, increasing the on-set and the flat band potential, thus hindering the charge transfer process. In addition, an ideal dopant can also control the morphology of the hematite photoanode (as a beneficial side effect).

Experimental methods

Chemicals and materials

Iron(III)acetylacetonate (99%), oleyl alcohol (85%), oleic acid (90%), germanium(IV)ethoxide (99%), and sodium hydroxide (99%) were purchased from Sigma-Aldrich. The chemicals and reagents were used as received without further purification.

Synthesis of magnetite nanoparticles (used in samples FeGe2 and pristine Fe)

We synthesized magnetite (Fe_3O_4) NCs following the protocol developed by Gonçalves *et al.*[33] We added 35 mL of oleyl alcohol and 8.0 mmol of iron(III)acetylacetonate into a reaction vessel (a 100 mL three-necked round-bottomed flask). The flask was thereafter heated at 100 °C under vacuum for 15 min for complete solubilization of iron(III)acetylacetonate. Subsequently, the vessel was heated at 320 °C under N_2 atmosphere for 60 min. Thereafter, the colloidal solution formed was allowed to cool to room temperature. The NCs formed were washed three times with acetone and re-dispersed in toluene, yielding a colloidal dispersion with a concentration of 400 mg mL^{-1}.

Synthesis of Ge-doped magnetite nanoparticles (used in the sample FeGe1)

The Ge-doped magnetite (Fe_3O_4) NC was prepared as follows: 35 mL of oleyl alcohol and 8 mmol of iron(III)acetylacetonate were put in a three-necked round-bottomed flask (100 mL). The flask was heated at 100 °C under vacuum for 15 min to completely solubilize iron(III)acetylacetonate. At this stage, we added 2 mL of an oleic acid solution containing 0.135 mmol of germanium(IV)ethoxide ([Ge]/([Ge] + [Fe] = 0.017)), and the reaction vessel was heated at 320 °C under N_2 atmosphere for 60 min. Thereafter, the colloidal solution formed was allowed to cool to room temperature. The NC formed was precipitated three times with acetone and re-dispersed in toluene, yielding a colloidal dispersion with a concentration of 400 mg mL^{-1}.

Magnetite nanoparticles contain Ge precursor preparation (used for FeGe2 sample)

To prepare FeGe2 sample, we added 0.0902 mmol of germanium ethoxide ([Ge]/([Ge] + [Fe] = 0.017)) to the colloidal

solution of undoped magnetite NC (400 mg of magnetite − 1.73 mmol) under N_2 atmosphere. The colloidal dispersion was homogenized in an ultrasonic bath for 30 min.

Thin films preparation

The thin films were prepared through the CND process using a spin-coating deposition procedure as follows: a commercial FTO substrate was used for the film deposition. Initially, the substrates were washed with soap, isopropyl alcohol, acetone, and toluene. Pure magnetite, Ge-doped magnetite, and colloidal solutions of magnetite and Ge precursors were deposited through spin-coating at a fixed rotation speed of 10 s (5000 rpm). After deposition, the films were sintered in a tubular furnace at 850 °C for 4 min for materials containing Ge and 20 min for undoped hematite.

Photoelectrochemical characterization

Photoelectrochemical measurements were performed in a standard three-electrode cell with the hematite film as the working electrode (0.28 cm^2 area), Ag/AgCl in a KCl saturated solution as the reference electrode, and a platinum plate as the counter electrode. 1.0 M NaOH solution (NaOH ACS Aldrich, 99.99%) in highly pure water (pH = 13.6, at 25 °C) was used as the electrolyte. A scanning potentiostat (potentiostat/galvanostat μAutolab III) was used to measure the dark and illuminated currents, at a scan rate of 20 mV s^{-1}. Sunlight (100 mW cm^{-2}) was simulated using a 250 W ozone-free xenon lamp (Osram) and an AM 1.5 filter (Newport Corp). Several electrochemical experiments assisted by a sunlight simulator were conducted using electrolytes with the addition of H_2O_2 as a hole scavenger (using an aqueous electrolyte solution prepared with 1 M NaOH + 0.5 M H_2O_2). IMPS measurements were performed in a three-electrode cell using a Metrohm Autolab PGSTAT302N/FRA2 setup, utilizing a 470 nm high-intensity blue LED for both the bias light intensity and sinusoidally modulated light. The modulation frequency ranged from 10 000 to 0.1 Hz, with a modulation amplitude of approximately 10% of the base light intensity, and the linearity of the response was tested and confirmed using Lissajous plots. The IMPS spectra were normalized by determining the number of modulated photons.

For the Mott–Schottky analysis, a Nyquist plot was constructed from 1.75 V_{RHE} to 0.8 V_{RHE} for both doped and undoped hematite, at a frequency of 1 kHz. Eqn (1) and Mott–Schottky plots were used to determine the donor density (N_d).

$$\frac{1}{C^2} = \frac{2}{\varepsilon_0 \varepsilon_r e N_d}\left(V - V_{fb} - \frac{k_B T}{e}\right), \quad (1)$$

where ε_0 denotes the permittivity under vacuum, ε_r is the relative permittivity (hematite was taken as 80),[34] V is the applied potential, T is the absolute temperature, e is the electronic charge, and k_B is Boltzmann's constant. UV-vis absorption spectra were obtained using a Shimadzu UV-3600 plus spectrophotometer.

The absorbed photocurrent density J_{abs} was calculated as expressed in eqn (2) as follows:

$$J_{abs} = q\int_{350}^{600} f(\lambda)A(\lambda)d\lambda, \quad (2)$$

where q denotes the electron charge, $f(\lambda)$ is the irradiance spectrum (in units no. of photons cm^{-2} nm^{-1} s^{-1}) of the light source used for photoelectrochemical measurements (AM 1.5 – 100 mW cm^{-2}), and $A(\lambda)$ is the absorptance spectrum of the pristine Fe and FeGe1 samples.

The APCE measurements were performed using 470, 532, and 627 nm high-intensity LED irradiation and can be expressed as follows:

$$\text{APCE } (\%) = \frac{1240 J_{photo}/E(\lambda)\lambda}{1 - 10^{A}} \times 10, \quad (3)$$

where J_{photo} denotes the photocurrent density (mA cm^{-2}), $E(\lambda)$ is the irradiance of the LED (mW cm^{-2}), λ is the LED wavelength, and A is the absorbance of the LED wavelength used.

Characterization

The thin films were characterized through XRD (Bruker, D8 Advance ECO) using CuKα radiation (λ = 0.15406 nm), linear detector LYNXEYE XE (PSD of 2.948°), primary optics (2.5° axial soller and 0.6 mm slit), and secondary optics (2.5° axial soller and 5.4 mm slit). TEM, HAADF-STEM, and EDS analyses were performed at 300 kV using a Titan Themis instrument with Cs correction. The analyses were performed with a spatial resolution greater than 0.1 nm. The TEM STEM/EDS sample was prepared *via in situ* milling using a focused ion beam system. Chemical surface analyses were performed by an XPS (Thermo Fisher Scientific, UK) using Al–Kα X-rays under vacuum (>10^{-8} mbar) and charge compensation during the measurements. A resolution of 1 eV with five scans was used to gather the survey spectra, where high-resolution spectra were recorded with 0.1 eV resolution and 50 scans. The binding energies were referenced to the C 1s peak at 284.8 eV. Data analysis was performed using the Thermo Scientific™ Avantage™ software. The C-AFM measurements were performed using an AFM microscope (Park Systems NX10) under a N_2 atmosphere with a tip nanosensor PPP-EFM Pt/Ir silicon coating with 75 kHz–2.8 N m and 25 nm of radius. The scan head was mounted within an environmental chamber maintained at constant relative humidity and temperature (<10% RH and 25 °C).

Results and discussion

As described in Scheme 1, two different approaches were employed to incorporate Ge into hematite. In the first route (FeGe1), Ge was introduced during the synthesis of Fe_3O_4 nanocrystals (NCs) (Scheme 1a). After the synthesis, the Ge-doped Fe_3O_4 NC was deposited through spin-coating onto fluorine-doped-SnO_2 (FTO) glass substrates, followed by a sintering process that promotes the formation of a hematite photoanode with a gradient of Ge concentration [Ge]. From this route, it is expected that the surfaces of the hematite grains are rich in Ge, with a gradual reduction in the [Ge] concentration moving away from the surface towards the hematite grain core as shown in Scheme 1a. For more details, refer to the

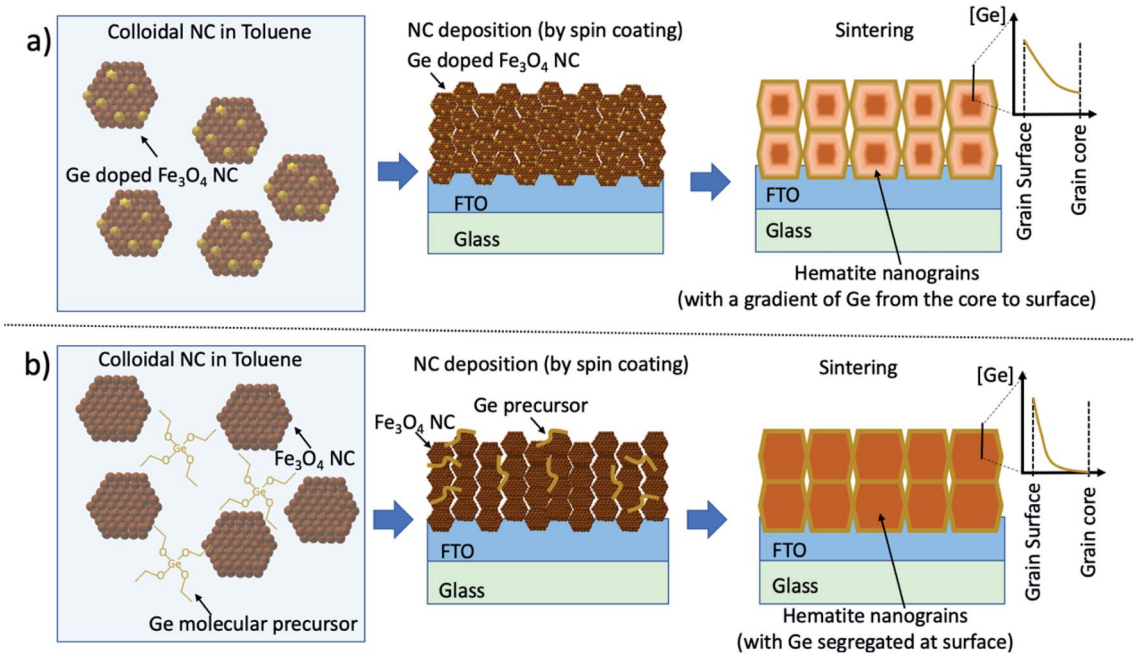

Scheme 1 Schematic of the routes used to process Ge-doped hematite photoanode. (a) In route FeGe1, Ge is introduced during the synthesis of Fe_3O_4 nanoparticle; (b) in route FeGe2, Ge is introduced after the synthesis of Fe_3O_4 NC. The sintering process leads to the hematite photoanode formation with preferential Ge segregation in the hematite grains surface as shown in (b).

experimental procedure. In the second route (FeGe2), Ge was added as a molecular compound that was soluble in toluene after the synthesis of Fe_3O_4 NCs (Scheme 1b). Herein, the sintering process led to the formation of hematite, with Ge preferentially segregating at the hematite grain surface as shown in Scheme 1b. The details of the synthesis protocol can be found in the Experimental methods.

As shown in Scheme 1, after NC preparation and deposition onto FTO, a sintering process at 850 °C was performed. At this stage, systematic efforts were devoted to optimize the parameters related to photoanode processing, such as Ge concentration, number of deposited layers, and time sintering treatment. In this process, the photocurrent density (J_{PH}) at 1.23 V_{RHE} was used as a figure of merit, aiming at its maximization. The parameter optimization achieved by studying the photoanodes designed following route FeGe1 was used to fabricate photoanodes *via* route FeGe2. Details regarding the optimization of the parameters can be found in the ESI (Tables S1–S3).† As a result of this study, it was established that the optimal nominal Ge concentration is 1.7 at%. Then, the optimized photoanodes were fabricated by two cycles of deposition processing followed by sintering at 850 °C for 4 min. An undoped hematite photoanode (pristine Fe), as a reference for performance, was prepared as reported in previous studies,[21,22] which involved a single deposition step and thermal treatment at 850 °C for 20 min. Thus, all analysis presented in this study are related to the samples prepared under these conditions.

Because the incorporation of Ge during the synthesis process is an important step in the route used, we performed a detailed characterization of the NC. Fig. 1 shows the scanning transmission electron microscopy (STEM) analysis of the nanoparticles produced through FeGe1 route. This approach allowed us to obtain nanoparticles with controlled shape (equiaxial) and size (mean particle size of 7 nm), as illustrated in the STEM high-angle annular dark-field (HAADF) image in Fig. 1a. Fig. 1b and c shows that these nanoparticles had a high degree of crystallinity (refer to the high-resolution HAADF image in Fig. 1b). The fast Fourier transform (FFT) analysis (Fig. 1c) of the oriented nanoparticles (Fig. 1b) shows an orientation along the [111] axis zone, and it presents the symmetry of the magnetite phase (Fe_3O_4). Elemental chemical analysis, performed by energy dispersive analysis (EDS) coupled with STEM (EDS-STEM), demonstrated that Ge was incorporated in Fe_3O_4 nanoparticles (Fig. 1d and insets), with a concentration of 1.7 at% of Ge. It is observed from the EDS map (Fig. 1d) and line profile analysis (refer to the inset in Fig. 1d) that Ge was homogeneously dispersed through the nanoparticles, with no sign of segregation. The protocol used in FeGe2 route was followed to prepare the undoped Fe_3O_4 NC, resulting in similar phase, morphology, and size, as revealed by transmission electron microscopy (TEM) analysis (refer to Fig. S2 in the ESI†). The undoped Fe_3O_4 nanoparticles were used to obtain a dopant-free hematite photoanode (referred to as Fe pristine).

We performed X-ray photoemission spectroscopy (XPS) analysis in the FeGe1 and FeGe2 samples (before the sintering process). As we can notice, the sample with Ge-ethoxide (route FeGe2) shows a [Ge]/([Ge] + [Fe]) ratio equal to 0.31, *i.e.*, much higher than the nominal amount added. This result suggests that most of the Ge is located outside the magnetite particles and is not in a solid solution. Moreover, the sample in which Ge was incorporated during the magnetite nanoparticle synthesis

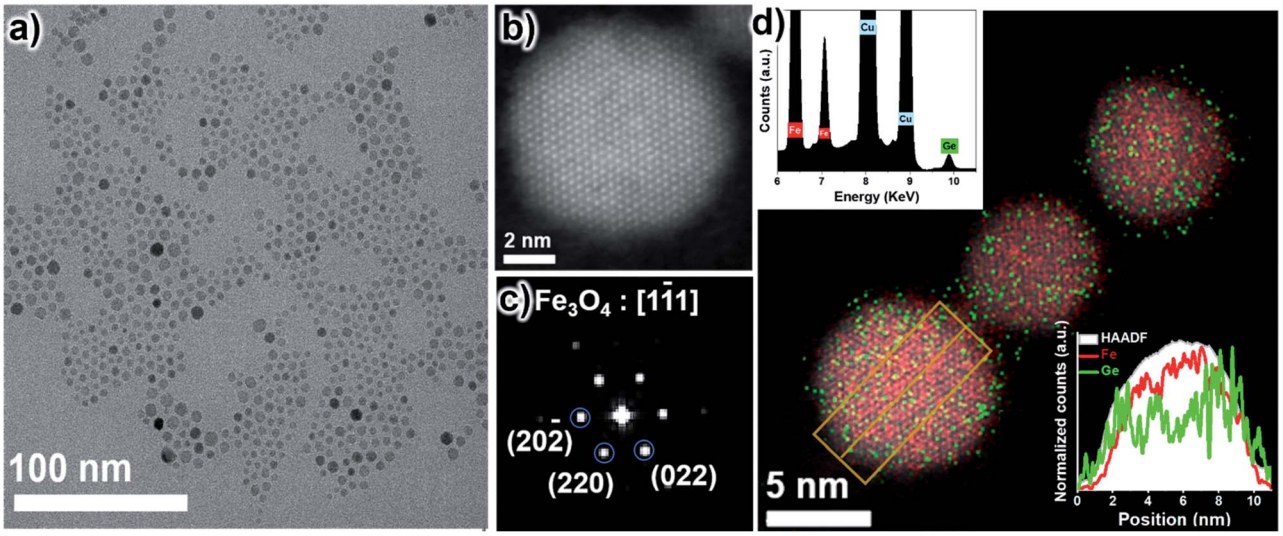

Fig. 1 STEM characterization of Fe_3O_4 nanoparticle used in route FeGe1. (a) Low magnification HAADF-STEM image of Ge-doped Fe_3O_4 nanoparticles; (b) high resolution HAADF-STEM image of Ge-doped Fe_3O_4 nanoparticle oriented along the [111] zone axis; (c) FFT of (b); (d) EDS-STEM map analysis of Ge-doped Fe_3O_4 nanoparticles. Insets illustrate the EDS spectrum and the line profile analysis, showing the HAADF, Ge, and Fe signals.

(route FeGe1) shows a [Ge]/([Ge] + [Fe]) ratio equal to 0.016, which is close to the nominal one, corroborating the EDS analysis (the nominal [Ge]/([Ge] + [Fe]) ratio is equal to 0.017).

Doped and non-doped hematite photoanodes were systematically characterized to comprehend their chemistry, structure, and morphology. X-ray diffraction (XRD) analyses, illustrated in Fig. 2a, for all sintered photoanodes exhibited a complete phase transformation from magnetite to hematite after the sintering process. The diffraction peaks were indexed to the hematite phase (JCPDS no. 33-0664) with preferential orientation along the [110] direction for the Fe-pristine and Ge-doped photoanodes (FeGe1 and FeGe2). No Ge-rich phase was identified after the sintering process; only the diffraction peaks assigned to SnO_2 (JCPDS no. 41-14445) were found to be associated with the FTO substrate.

The atomic force microscopy (AFM) image of the sintered photoanode, shown in Fig. 2b–d, illustrates that the presence of Ge (samples FeGe1 and FeGe2) promotes a significant reduction in the grain size of the pristine Fe photoanode. Because the initial magnetite NC size ranged from 3 to 8 nm (refer to the TEM analysis in Fig. 1 and S2 in the ESI†), an extensive oriented growth process occurred during thermal treatment. This oriented growth process led to the formation of a columnar morphology with textured hematite grains oriented along the [110] direction, as indicated by the XRD results and illustrated in the HAADF STEM image shown in Fig. 2e and f. Moreover, the suppression of grain growth due to the presence of Ge suggests segregation at the hematite grain surface during the sintering process.[35] To assess the degree of Ge segregation on the surface of the hematite grains, XPS measurements were performed (refer to Fig. S3†). From the XPS analysis, the [Ge]/([Fe] + [Ge]) atomic ratio was estimated at approximately 0.32 and 0.42 for FeGe1 and FeGe2 samples, respectively, which are higher than the nominal ratio ([Ge]/([Fe] + [Ge]) = 0.017), indicating a high degree of the Ge^{4+} segregation over the hematite grains surface.

The GeO_2 chemical, which is highly soluble in basic solutions, was explored after the sintering process.[36] Ge-doped hematite photoanodes (FeGe1 and FeGe2) were immersed in 1 M NaOH water solution (pH 13.6) for 60 min. The photoanodes were thereafter washed with ultra-pure water and subjected to XPS, STEM-EDS, and photoelectrochemical measurements. XPS analysis exhibited a significant reduction of the [Ge]/([Fe] + [Ge]) atomic ratio after treatment in basic solution (from 0.32 to 0.28 for FeGe1 and from 0.42 to 0.13 for FeGe2), indicating that part of Ge^{4+}, present in the hematite grains surface, was leached. STEM-EDS analysis performed on FeGe1 photoanode before and after the leaching treatment, illustrated in Fig. 2e and f, clearly shows the elimination of the Ge present in the hematite pore surface, agreeing well with the results of the XPS analysis.

To evaluate the impact of the added Ge on the performance of the hematite photoanode, photoelectrochemical measurements were performed under standard AM 1.5 G irradiation. The *J–V* curves obtained for the photoanodes illuminated on the front side of the electrochemical cell are shown in Fig. 3a. The Ge–hematite photoanodes exhibited a high photocurrent response compared to the pristine Fe photoanode. The best performance in terms of J_{PH} (J @ 1.23 V *vs.* RHE) was achieved by photoanode FeGe1 (J_{PH} = 3.2 mA cm^{-2}). This photocurrent value is one of the best among the reported high-performance hematite photoanode systems without multiple modifications, such as deposition of an overlayer to act as a passivating or co-catalyst layer, or modification of the FTO/hematite interface.[5] The high solubility of GeO_2 in concentrated NaOH solution may raise doubts regarding the stability of this photoanode. However, chronoamperometry tests (see Fig. S4, in the ESI†)

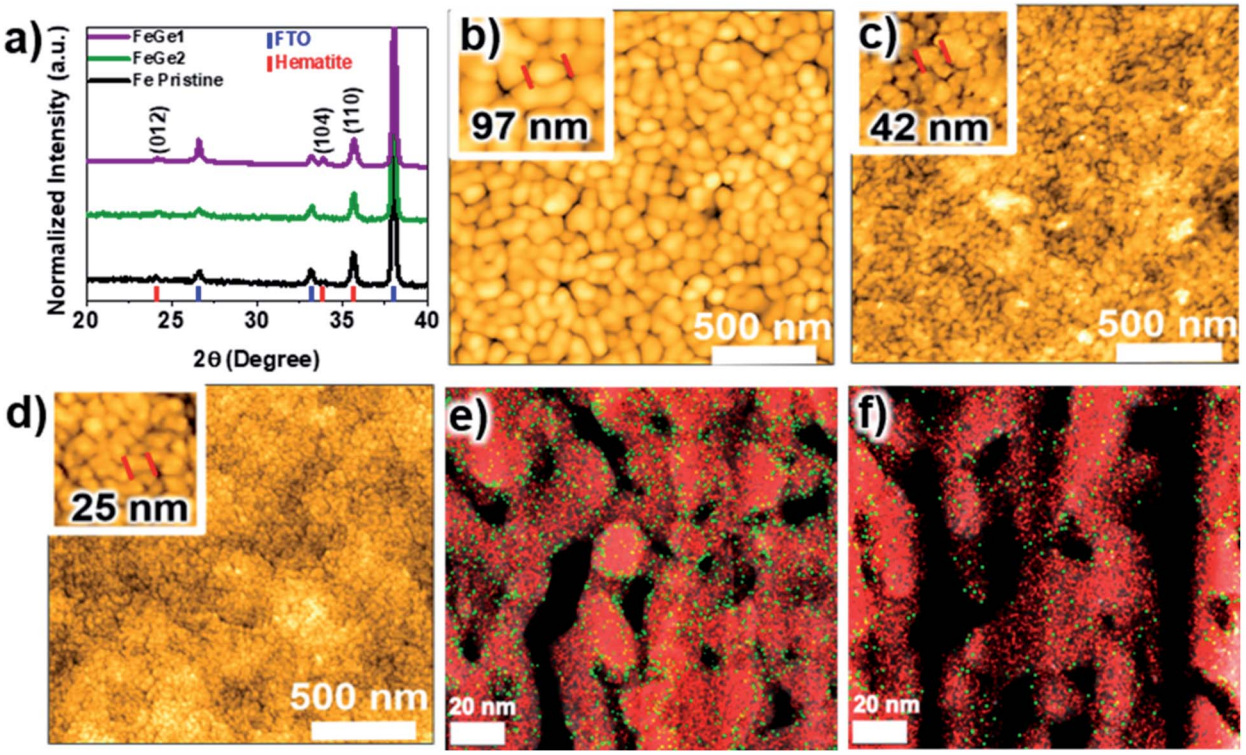

Fig. 2 Combination of structural and microscopy characterization. (a) XRD analysis of FeGe1, FeGe2, and pristine Fe films; (b–d) shows non-contact topological AFM images of pristine Fe, FeGe2, and FeGe1 films, respectively. The insets show high magnification AFM images, highlighting the grain size; (e) and (f) superposition of HAADF-STEM image with EDS map for FeGe1 before (e) and after (f) the leaching treatment of the film in basic water solution (pH 13.6). The EDS-STEM images show the elemental distribution of Fe (red) and Ge (green).

reveal that this system has high stability, with negligible photocurrent variation as a function of time.

To understand the role of Ge in the PEC properties of the hematite photoanode regarding its water oxidation efficiency, Mott–Schottky analysis was performed for the pristine Fe and FeGe1 photoanodes. The Mott–Schottky plots for both photoanodes, illustrated in Fig. 3b, have positive slopes, indicating that electrons are the majority carriers, and we estimated the donor density (N_d) value from this plot. Because V_{fb} is an important parameter in our future analysis, we need to have confidence in this value. Thus, we determined V_{fb} based on the Gärtner–Butler analysis in the presence of a sacrificial reagent (H_2O_2; refer to the details in Fig. S5 in ESI†) to increase the confidence of this measurement.[37] Both N_d and V_{fb} values are summarized in Table 1. It is observed that the N_d value for FeGe1 photoanode is approximately 1.5 times greater than the values estimated for the pristine Fe photoanode. The estimated quantities considering the Mott–Schottky model have been constantly addressed in previous studies based on their inherent uncertainties to describe materials at the nanometric scale.[38,39] Thus, the observed difference in the N_d values was considered negligible. However, the addition of Ge promotes a small shift in V_{fb} (refer to Table 1), unlike other dopants such as Sn and Sb that cause a sensitive anodic shift in V_{fb}.[21,22]

To gain more insight into the performance of the photoanode, we calculated the absorbed photocurrent density (J_{abs}, considering 100% quantum yield) and overall efficiency ($\eta_{overall} = J_{PH}/J_{abs}$) for the pristine Fe and FeGe1 photoanodes. We listed the results in Table 1. The values of J_{abs} were calculated from the ultraviolet-visible (UV-vis) spectra (refer to Fig. S6 and the details in ESI†). Table 1 summarizes the $\eta_{overall}$ values, demonstrating that FeGe1 photoanode is five times higher than that of the undoped photoanode. Although these two systems exhibited similar light-harvesting efficiencies (J_{abs}), their overall efficiencies were significantly different.

To better understand the role of Ge in the charge carrier dynamics of hematite photoanodes, we performed intensity-modulated photocurrent spectroscopy (IMPS) measurements. Fig. 3c shows the IMPS plot for the pristine Fe and FeGe1 photoanodes measured from 0.56 to 1.46 V *vs.* RHE under blue light-emitting diode (LED) irradiation. For the pristine Fe hematite (Fig. 3c, top), it is clearly observed that at high frequencies (ω), the IMPS transfer function (H) values are close to zero; as the frequency decreases, the H data points form a semicircle in the fourth quadrant until they intercept the real axis at the intermediate frequency, which represents the charge separation efficiency at a given light-harvesting efficiency (LHE), neglecting the surface recombination and charge transfer, as expressed in eqn (1) as follows:[41–43]

$$\text{Intercept}_{w\ \text{intermediate}} = \text{CSE} \times \text{LHE} \quad (4)$$

$$\text{Intercept}_{w\to 0} = \text{EQE} \quad (5)$$

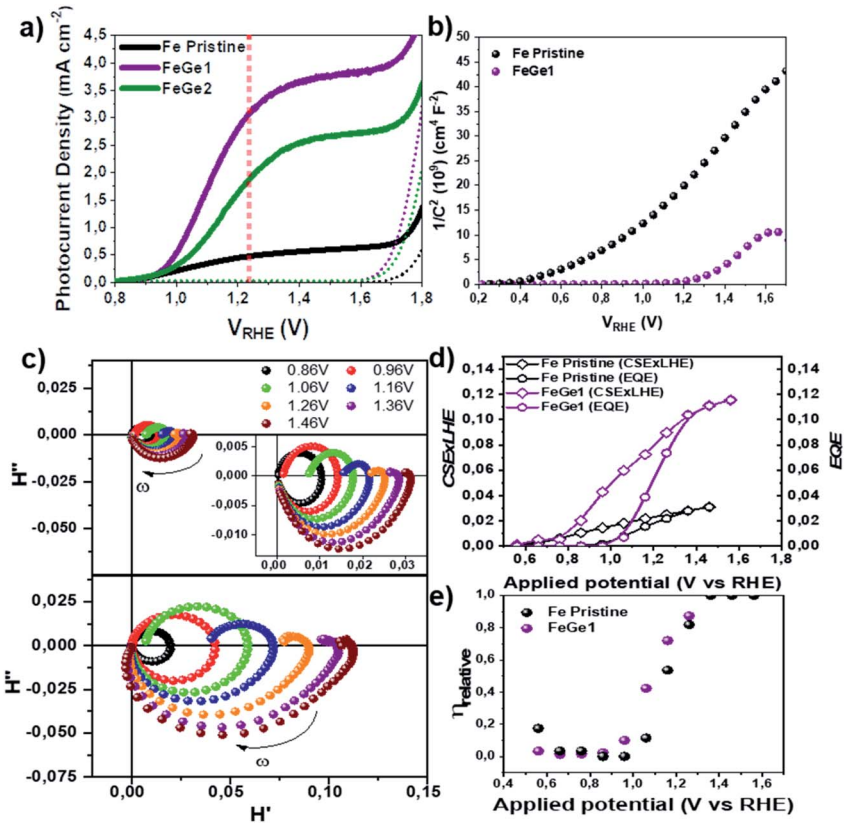

Fig. 3 Photoelectrochemical characterization of the pristine and Ge-doped hematite photoanodes. (a) Current density *versus* potential curves ($J \times V_{RHE}$) measured in darkness and under illumination for the pristine Fe, FeGe1, and FeGe2 samples. This experiment was conducted using an aqueous electrolyte with 13.6 pH (NaOH solution) and 100 mW cm^{-1} light intensity; (b) Mott–Schottky plots measured at 1 kHz frequency in 1 M NaOH solution in darkness for the pristine Fe and FeGe1 samples; (c) IMPS spectra obtained for pristine hematite and Ge–hematite at the potentials indicated under front-side illumination using a blue LED (470 nm) in a 1 M NaOH aqueous solution. Potential dependence of (d) charge separation efficiency at a given light harvesting efficiency (CSE × LHE) and external quantum efficiency (EQE) and (e) relative hole transfer efficiency (η_{rel}) obtained from IMPS plots.

At lower frequencies, a second semicircle that depended on the applied potential was obtained in the first quadrant. As the applied voltage increases, the intercept at low frequency, which is also associated with the external quantum efficiency (EQE, eqn (2)), moves away from the origin, thereby increasing the photocurrent, as also observed in the *J*–*V* curves. At $V > 1.26$ V, the first quadrant semicircle disappears, indicating that the hole transfer is significantly faster than the surface recombination.[44] A similar trend is observed for FeGe1 film (Fig. 3c, bottom) at the same potential ranges in which both semicircles are clearly distinguished from 0.8 to 1.26 V. Interestingly, at more positive potentials and high frequencies, the IMPS function crosses from the third to the fourth quadrant, suggesting that the Ge insertion increases the electron diffusion length in hematite.[45]

Although the IMPS measurements of both films present a similar potential dependence, it is clearly noted that the intercepts, CSE × LHE and EQE (eqn (1) and (2)), are significantly different. Fig. 3d shows the CSE × LHE and EQE values extracted from Fig. 3c as a function of the applied potential. Ranging from 0.5 to 0.8 V, the achieved CSE × LHE values are equivalent for both photoanodes, indicating an equal separation efficiency in this range. As the potential increased, the CSE × LHE of FeGe1 film became superior to that of the pristine

Table 1 J_{abs}, J_{PH}, $\eta_{overall}$ ($\eta_{overall} = J_{PH}/J_{abs}$), N_d, and V_{fb} for pristine Fe and FeGe1 samples that exhibited the highest photocurrent response during sunlight-assisted water oxidation. N_d value was estimated from the Mott–Schottky plot, and V_{fb} from the Gärtner approach.[37,40] J_{abs}, J_{PH}, and $\eta_{overall}$ were determined from optical and photo-electrochemical measurements

Sample	J_{abs} (mA cm^{-2})	J_{PH} (@ 1.23 V *vs.* V_{RHE}) (mA cm^{-2})	$\eta_{overall}$ (J_{PH}/J_{abs})	N_d (cm^{-3}) ($\times 10^{19}$)	V_{fb} (V/V_{RHE})
Pristine Fe	10.1	0.5	0.05	3.9	0.68
FeGe1	11.7	3.2	0.27	5.9	0.78

hematite, reaching higher values (~6× at 1.46 V). The reason for this difference will be explained later. For EQE, both films exhibited values close to zero ranging from 0.5 to 0.96 V; at more positive potentials, an increasing trend is noticeable until EQE becomes equal to CSE × LHE at $V >$ than 1.3 V. Interestingly, an area between CSE × LHE and EQE is observed for both films, indicating that, ranging from 0.5 to 1.25 V, an important portion of photogenerated holes are lost through surface recombination.

The IMPS spectra were also analyzed to extract the transfer and surface constants (k_{tr} and k_{sr}), and consequently, calculate the relative hole transfer efficiency (η_{rel}), defined as the ratio between k_{tr} and ($k_{tr} + k_{sr}$). The identical values and trends of η_{rel}, displayed in Fig. 3e, show that the surface of the two photoanodes (Fe pristine and FeGe1) present surfaces with similar behavior, concerning the charge transfer process. Thus, after the leaching treatment, the surface charge transfer processes in the FeGe1 photoanode are dominated by the new hematite surface (with residual Ge), which must be like those of the pristine Fe hematite surface.

Based on previous results, the addition of Ge should improve the charge carrier separation process, increasing the conductivity of the majority carriers (e^-). To evaluate this hypothesis, conductive AFM (C-AFM) analysis was performed for the pristine Fe and FeGe1 photoanodes, as shown in Fig. 4a and b, respectively. In C-AFM, an electrically conductive tip is placed in contact with the photoanode surface, thereby completing a circuit and allowing charge transfer through different regions of the photoanodes (refer to Fig. 4a). A simple qualitative analysis of the C-AFM images shows that FeGe1 photoanode has a higher conductivity (represented by the high current and bright area in Fig. 4c) than the pristine Fe photoanode (Fig. 4b). However, a semiquantitative estimation of this conductivity can also be performed. Because the same conductive tip was used to perform the C-AFM measurements of both photoanode surfaces, the current density (J in nA nm^{-2}) can be estimated by considering the average value of the current in the analyzed area. Considering the applied electric field (E) (v/film thickness), the ratio between the conductivity of the pristine Fe (σ_{FeP}) and FeGe1 (σ_{FeGe1}) photoanodes (remembering that $J = \sigma E$) was estimated. This analysis demonstrates that $\sigma_{FeGe1} \sim 34\sigma_{FeP}$. The electronic conductivity of the Ge-modified sample was more than one order of magnitude higher than that of the pristine sample.

The conductivity can be described as the product of the concentration (N_d) and mobility (μ) of charge carriers (q): $\sigma = (N_d q)\mu$. Revisiting the Mott–Schottky results obtained in this study, the addition of Ge does not result in an increase in N_d. Thus, Ge addition can be associated with a gain in the mobility of the majority carriers (e^-). Considering the values of N_d and the relationship between $\sigma_{FeGe1} \sim 34\sigma_{FeP}$, the electron mobility for FeGe1 photoanode was estimated to range from 22 to 34 times higher than that for the pristine Fe photoanode.

The improvement in carrier mobility due to the doping effect has been reported in previous studies proposed that the high performance of Ti-doped hematite photoanodes is associated with an increase in N_d and a prolonged carrier lifetime.[46,47] More recently, Zhang *et al.*[48] using a combination of solid-state electronic transport and PEC characterizations, reported that the improvement of electron transport and charge carrier efficiency in Mo-doped $BiVO_4$ is due to the lowered small polaron hopping barrier. Similarly, Pastor *et al.*[49] proposed that the deleterious effect and polaronic states formation could be avoided during the materials fabrication process for PEC applications.[25] The origin of the low electron mobility in hematite can be attributed to the high localization of small polarons[18,50] that require a high activation energy to hop to the adjacent atom. The addition of Ge to hematite should affect the degree of localization of the small polarons, boosting their transport and photocurrent. Because the small polaron localization of the photoexcited carrier is wavelength-dependent, we used the absorbed photon-to-current conversion efficiency (APCE) to understand the effect of Ge on the carrier mobility of hematite. The APCE as a function of potential was determined (for details about the APCE calculation, refer to the experimental procedure) by considering three different wavelengths. Because the localization effect of small polarons is more pronounced in the wavelength near the hematite band edge, the excitation at an energy slightly higher than the bandgap (where there is an efficient small polaron formation) and two other energies where a mixture between polaron formation and charge mobility occurs were selected.[5,19,37,49] Considering that most of the charge separation process in hematite occurs in the depletion layer region, that is, for $V_{RHE} > V_{fb}$, we corrected the applied potential V_{RHE} by V_{fb} ($V_{RHE} - V_{fb}$). The results are shown in Fig. 4d–h. The addition of Ge (FeGe1 photoanode) resulted in a significantly higher APCE value, regardless of the excitation wavelength used to perform the measurements. At 627 nm excitation (Fig. 4d), we observed that FeGe1 and pristine Fe photoanodes exhibited an APCE signal only for $V_{RHE} > V_{fb}$. However, we note that the undoped photoanode (pristine Fe) requires a higher anodic potential for the water oxidation process to occur, demonstrating that the localization effect of small polarons is more pronounced in this sample. This result strongly indicates that the addition of Ge modified the formation of small polarons, thus increasing the lifetime of the carriers. At more energetic excitations (532 and 470 nm, as shown in Fig. 4e–h), we observed a significant increase in the APCE as a function of potential, clearly indicating an increase in the mobility of charge carriers. Moreover, we noticed that the sample with Ge (FeGe1) presents an APCE signal even at a potential lower than V_{fb} (refer to Fig. 4g and h), suggesting that we can extract charges close to the surface of hematite, even without the aid of band bending. The pristine Fe sample exhibited only an APCE signal at $V_{RHE} > V_{fb}$, even for more energetic excitations.

Finally, we discuss the effect of grain size reduction after the sintering step, promoted by the addition of Ge (a side effect), on the photoelectrochemical performance. As illustrated in Fig. S7a (refer to the ESI),† most of the photocurrent was generated at $V_{RHE} > V_{fb}$, indicating that the charge separation process occurred mostly in the depletion layer width (W). Fig. S7b† shows the evolution of W (assuming classical depletion layer theory[2,3]) as a function of the applied potential for the pristine Fe and FeGe1 photoanodes. As the two samples differ in

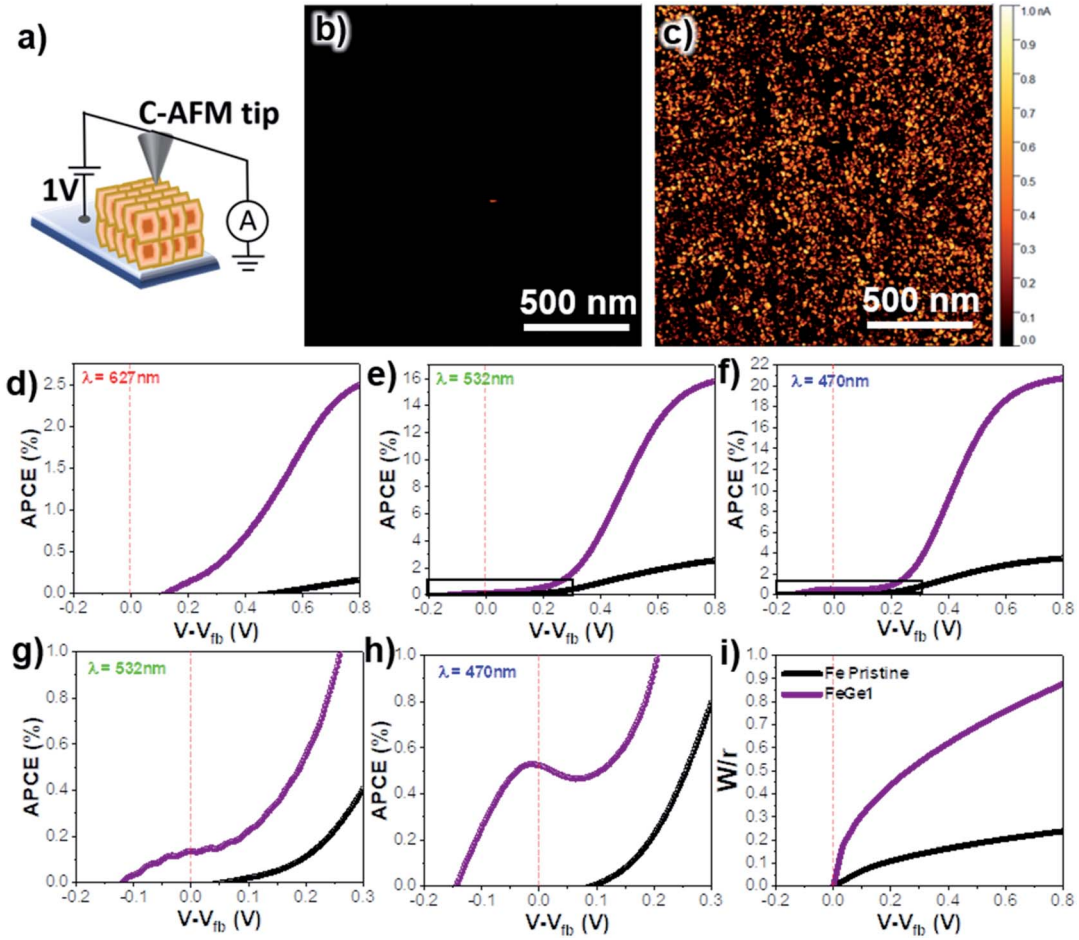

Fig. 4 C-AFM, APCE, and depletion layer width (W) analysis for the pristine Fe and FeGe1 photoanodes. (a) Schematic of the experimental set-up used to perform the measurement of C-AFM; (b) C-AFM image of the pristine Fe photoanode; (c) C-AFM image of FeGe1 sample; (d) APCE measurement as a function of the correctly applied potential ($V-V_{fb}$) measured with an excitation of 627 nm; (e) APCE measurement as a function of ($V-V_{fb}$) measured with an excitation of 532 nm; (f) APCE measurement as a function of ($V-V_{fb}$) measured with an excitation of 470 nm; (g) zoom of the APCE curve (highlighted area) of (e); (h) zoom of the APCE curve (highlighted area) of (f); and (i) W normalized by the characteristic morphological feature size (W/r_G, where r_G denotes the mean grain radius) as a function of ($V-V_{fb}$).

morphology, mainly grain size (refer to Fig. 2b–d and S3 in ESI†), a direct comparison between the samples becomes unfeasible. Thus, we normalized W by a characteristic morphological feature size (mean grain radius, r_G), and the results are plotted in Fig. 4i. The W/r_G ratio is a parameter related to the active volume fraction of the hematite used in the light-assisted water splitting process.[51] We observed that the reduction in the grain size caused by the addition of Ge led to better use of the active volume fraction of the material (a higher W/r_G ratio) when compared to non-doped hematite.

Conclusions

The results presented here demonstrate that the strategy of using Ge doping during nanoparticle synthesis (FeGe1 route) is fundamental for obtaining a high-performance photoanode. Moreover, we believe that efficient doping with Ge became viable because magnetite was used as the hematite precursor. Magnetite has an inverted spinel-like cubic structure that is more tolerant to the formation of defects than the corundum-like structure of hematite.[52] With the phase transformation during sintering, FeGe1 route allowed greater control of Ge dispersion, as demonstrated by the XPS data. After the leaching treatment, we reported the elimination of part of Ge. Thereafter, we observed (through IMPS measurements) that FeGe1 photoanode had a surface with similar behavior, concerning the charge transfer process, to that of the pristine Fe photoanode. Furthermore, C-AFM measurements clearly demonstrate that Ge improves the electronic conductivity and increases the majority carrier mobility. Measurements of APCE as a function of the applied potential, performed at varying excitation wavelengths, show that Ge interferes with the formation of small polarons, making the charges more mobile (delocalized), thus favoring the process of photoinduced charge separation. In addition, Ge helps to control the photoanode morphology by inhibiting grain growth during the sintering process. Based on these characteristics, we conclude that Ge is an ideal dopant for improving the charge separation in hematite photoanodes.

Author contributions

Murillo Henrique de Matos Rodrigues: investigation, data curation, formal analysis, writing – original draft, writing – review & editing, visualization. Ingrid Rodriguez-Guitierréz: formal analysis, writing – review & editing. Carlos Alberto Ospina Ramirez: formal analysis. Carlos Alberto Rodrigo Costa: formal analysis. Cleyton Alexandre Biffe: formal analysis. João Batista de Souza Junior: writing – review & editing, visualization. Flávio Leandro Souza: writing – review & editing, visualization. Edson Roberto Leite: conceptualization, writing – review & editing, supervision, funding acquisition.

Conflicts of interest

There are no conflicts to declare.

Acknowledgements

The authors acknowledge financial support from FAPESP (projects CEPID – 2013/07296-2, 2017/02317-2, 2017/03135, and 2018/05159-1), and CAPES – Finance Code 001 (process 88887.310931/2018-00). All Brazilian agencies are gratefully acknowledged.

References

1 A. J. Bard and M. A. Fox, *Acc. Chem. Res.*, 1995, **28**, 141–145.
2 M. G. Walter, E. L. Warren, J. R. McKone, S. W. Boettcher, Q. Mi, E. A. Santori and N. S. Lewis, *Chem. Rev.*, 2010, **110**, 6446–6473.
3 K. Sivula, F. Le Formal and M. Grätzel, *ChemSusChem*, 2011, **4**, 432–449.
4 I. S. Cho, H. S. Han, M. Logar, J. Park and X. Zheng, *Adv. Energy Mater.*, 2016, **6**, 1501840.
5 C. Li, Z. Luo, T. Wang and J. Gong, *Adv. Mater.*, 2018, **30**, 1707502.
6 S. D. Tilley, M. Cornuz, K. Sivula and M. Grätzel, *Angew. Chem., Int. Ed.*, 2010, **49**, 6405–6408.
7 H. Zhang, D. Li, W. J. Byun, X. Wang, T. J. Shin, H. Y. Jeong, H. Han, C. Li and J. S. Lee, *Nat. Commun.*, 2020, **11**, 4622.
8 Z. Luo, T. Wang, J. Zhang, C. Li, H. Li and J. Gong, *Angew. Chem., Int. Ed.*, 2017, **56**, 12878–12882.
9 Z. Zhang, H. Nagashima and T. Tachikawa, *Angew. Chem., Int. Ed.*, 2020, **59**, 9047–9054.
10 J. Y. Kim, G. Magesh, D. H. Youn, J.-W. Jang, J. Kubota, K. Domen and J. S. Lee, *Sci. Rep.*, 2013, **3**, 2681.
11 T. H. Jeon, G.-h. Moon, H. Park and W. Choi, *Nano Energy*, 2017, **39**, 211–218.
12 J. Li, H. Chen, C. A. Triana and G. R. Patzke, *Angew. Chem., Int. Ed.*, 2021, **60**, 18380–18396.
13 A. L. M. Freitas, D. N. F. Muche, E. R. Leite and F. L. Souza, *J. Am. Ceram. Soc.*, 2020, **103**, 6833–6846.
14 A. G. Hufnagel, H. Hajiyani, S. Zhang, T. Li, O. Kasian, B. Gault, B. Breitbach, T. Bein, D. Fattakhova-Rohlfing, C. Scheu and R. Pentcheva, *Adv. Funct. Mater.*, 2018, **28**, 1804472.
15 C. X. Kronawitter, I. Zegkinoglou, S. H. Shen, P. Liao, I. S. Cho, O. Zandi, Y. S. Liu, K. Lashgari, G. Westin, J. H. Guo, F. J. Himpsel, E. A. Carter, X. L. Zheng, T. W. Hamann, B. E. Koel, S. S. Mao and L. Vayssieres, *Energy Environ. Sci.*, 2014, **7**, 3100–3121.
16 M. Cornuz, M. Grätzel and K. Sivula, *Chem. Vap. Deposition*, 2010, **16**, 291–295.
17 S. C. Warren, K. Voïtchovsky, H. Dotan, C. M. Leroy, M. Cornuz, F. Stellacci, C. Hébert, A. Rothschild and M. Grätzel, *Nat. Mater.*, 2013, **12**, 842–849.
18 A. J. E. Rettie, W. D. Chemelewski, D. Emin and C. B. Mullins, *J. Phys. Chem. Lett.*, 2016, **7**, 471–479.
19 L. M. Carneiro, S. K. Cushing, C. Liu, Y. Su, P. Yang, A. P. Alivisatos and S. R. Leone, *Nat. Mater.*, 2017, **16**, 819–825.
20 J. B. Souza Junior, F. L. Souza, L. Vayssieres and O. K. Varghese, *Appl. Phys. Lett.*, 2021, **119**, 200501.
21 R. H. Gonçalves and E. R. Leite, *Energy Environ. Sci.*, 2014, **7**, 2250–2254.
22 A. E. Nogueira, M. R. Santos Soares, J. B. Souza Junior, C. A. Ospina Ramirez, F. L. Souza and E. R. Leite, *J. Mater. Chem. A*, 2019, **7**, 16992–16998.
23 M. R. S. Soares, C. A. R. Costa, E. M. Lanzoni, J. Bettini, C. A. O. Ramirez, F. L. Souza, E. Longo and E. R. Leite, *Adv. Electron. Mater.*, 2019, **5**, 1900065.
24 F. C. de Lima, G. R. Schleder, J. B. Souza Junior, F. L. Souza, F. B. Destro, R. H. Miwa, E. R. Leite and A. Fazzio, *Appl. Phys. Lett.*, 2021, **118**, 201602.
25 J. Liu, C. Liang, G. Xu, Z. Tian, G. Shao and L. Zhang, *Nano Energy*, 2013, **2**, 328–336.
26 L. Zhao, J. Xiao, H. Huang, Q. Huang, Y. Zhao and Y. Li, *Int. J. Hydrogen Energy*, 2018, **43**, 12646–12652.
27 P. Liao, M. C. Toroker and E. A. Carter, *Nano Lett.*, 2011, **11**, 1775–1781.
28 Z. Zhou, P. Huo, L. Guo and O. V. Prezhdo, *J. Phys. Chem. C*, 2015, **119**, 26303–26310.
29 J. Liu, C. Liang, H. Zhang, Z. Tian and S. Zhang, *J. Phys. Chem. C*, 2012, **116**, 4986–4992.
30 T. J. Smart, V. U. Baltazar, M. Chen, B. Yao, K. Mayford, F. Bridges, Y. Li and Y. Ping, *Chem. Mater.*, 2021, **33**, 4390–4398.
31 K.-Y. Yoon, J. Park, M. Jung, S.-G. Ji, H. Lee, J. H. Seo, M.-J. Kwak, S. Il Seok, J. H. Lee and J.-H. Jang, *Nat. Commun.*, 2021, **12**, 4309.
32 V. Agafonov, D. Michel, M. Perez y Jorba and M. Fedoroff, *Mater. Res. Bull.*, 1984, **19**, 233–239.
33 R. H. Gonçalves, B. H. R. Lima and E. R. Leite, *J. Am. Chem. Soc.*, 2011, **133**, 6012–6019.
34 J. H. Kennedy and K. W. Frese, *J. Electrochem. Soc.*, 1978, **125**, 723–726.
35 E. R. Leite, A. P. Maciel, I. T. Weber, P. N. Lisboa-Filho, E. Longo, C. O. Paiva-Santos, A. V. C. Andrade, C. A. Pakoscimas, Y. Maniette and W. H. Schreiner, *Adv. Mater.*, 2002, **14**, 905–908.
36 O. H. Johnson, *Chem. Rev.*, 1952, **51**, 431–469.
37 A. Hankin, F. E. Bedoya-Lora, J. C. Alexander, A. Regoutz and G. H. Kelsall, *J. Mater. Chem. A*, 2019, **7**, 26162–26176.

38 K. Sivula, *ACS Energy Lett.*, 2021, **6**, 2549–2551.
39 M. G. Walter, E. L. Warren, J. R. McKone, S. W. Boettcher, Q. Mi, E. A. Santori and N. S. Lewis, *Chem. Rev.*, 2011, **111**, 5815–5815.
40 W. W. Gärtner, *Phys. Rev.*, 1959, **116**, 84–87.
41 I. Rodríguez-Gutiérrez, R. García-Rodríguez, M. Rodríguez-Pérez, A. Vega-Poot, G. Rodríguez Gattorno, B. A. Parkinson and G. Oskam, *J. Phys. Chem. C*, 2018, **122**, 27169–27179.
42 I. Rodriguez-Gutierrez, J. B. Souza Junior, E. R. Leite, L. Vayssieres and F. L. Souza, *Appl. Phys. Lett.*, 2021, **119**, 071602.
43 C. Y. Cummings, F. Marken, L. M. Peter, A. A. Tahir and K. G. U. Wijayantha, *Chem. Commun.*, 2012, **48**, 2027–2029.
44 L. M. Peter, K. G. U. Wijayantha and A. A. Tahir, *Faraday Discuss.*, 2012, **155**, 309–322.
45 A. Bou, H. Āboliņš, A. Ashoka, H. Cruanyes, A. Guerrero, F. Deschler and J. Bisquert, *ACS Energy Lett.*, 2021, **6**, 2248–2255.
46 B. Zhao, T. C. Kaspar, T. C. Droubay, J. McCloy, M. E. Bowden, V. Shutthanandan, S. M. Heald and S. A. Chambers, *Phys. Rev. B: Condens. Matter Mater. Phys.*, 2011, **84**, 245325.
47 G. Wang, Y. Ling, D. A. Wheeler, K. E. N. George, K. Horsley, C. Heske, J. Z. Zhang and Y. Li, *Nano Lett.*, 2011, **11**, 3503–3509.
48 W. Zhang, F. Wu, J. Li, D. Yan, J. Tao, Y. Ping and M. Liu, *ACS Energy Lett.*, 2018, **3**, 2232–2239.
49 E. Pastor, J.-S. Park, L. Steier, S. Kim, M. Grätzel, J. R. Durrant, A. Walsh and A. A. Bakulin, *Nat. Commun.*, 2019, **10**, 3962.
50 Y. Fan, Y. Lin, K. Wang, K. H. L. Zhang and Y. Yang, *Phys. Rev. B*, 2021, **103**, 085206.
51 S. C. Warren, K. Voitchovsky, H. Dotan, C. M. Leroy, M. Cornuz, F. Stellaci, C. Hérbet, A. Rothschild and M. Graetzel, *Nat. Mater.*, 2013, **12**, 842–849.
52 R. M. Cornell and U. Schwertmann, in *The Iron Oxides*, 2003, pp. 9–38, DOI: **10.1002/3527602097.ch2**.